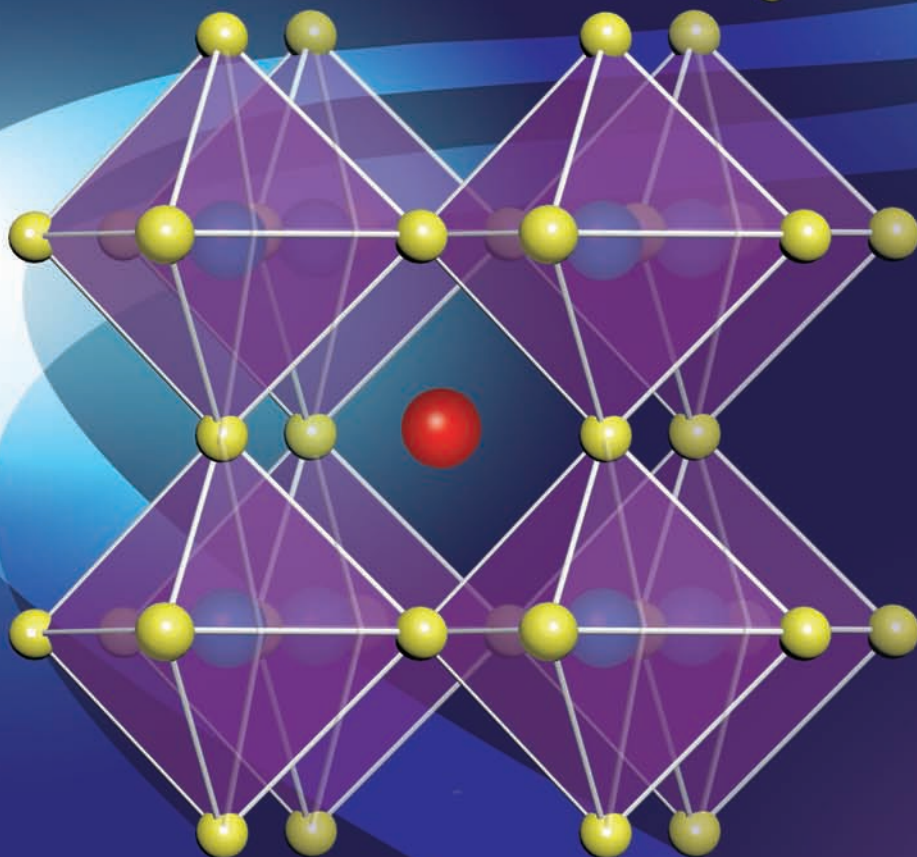
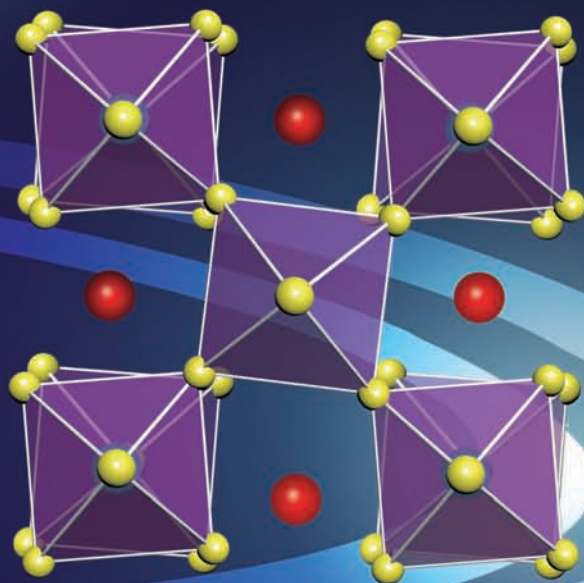
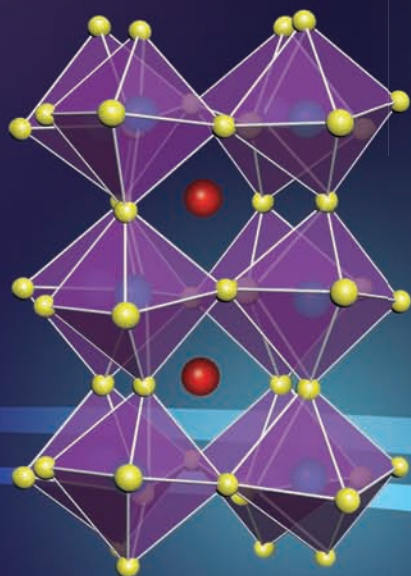


Vol. 5 • No. 14 • July 23 • 2018

www.advmatinterfaces.de

ADVANCED MATERIALS INTERFACES



WILEY-VCH

Interfacial-Field-Induced Increase of the Structural Phase Transition Temperature in Organic–Inorganic Perovskite Crystals Coated with ZnO Nanoshell

Fenghuan Zhao, Xian Gao, Xuan Fang, Yuri D. Glinka, Xiyuan Feng, Zhubing He,* Zhipeng Wei,* and Rui Chen*

The hybrid organic–inorganic perovskites are known to exhibit a complex crystalline structure, which allows for the structural phase transitions among the orthorhombic, tetragonal, and cubic phases that occur at different temperatures. This behavior of the organic–inorganic perovskites can significantly alter their optoelectronic properties. Here, using photoluminescence spectroscopy, it is shown that the structural orthorhombic-to-tetragonal phase transition temperature in MAPbI₃ perovskite crystal can be increased from 135 to 160 K upon coating with ZnO nanoshell. The phenomenon is attributed to the interfacial-field-induced atomic rearrangement in the near-surface area. The findings shed light on the great importance of the interfacial electric field effect on the structural and optical properties of the organic–inorganic perovskites, which hold great promise for their potential applications in the structural-phase-controlled optoelectronic and photovoltaic devices.

success as visible-light sensitizers for dye-sensitized solar cells, in recent years, the organic–inorganic halide perovskites have attracted great attention as a promising material for photovoltaic and light-emitting device applications.^[2–6] It was reported that the power conversion efficiency of MAPbX₃ perovskite solar cells has quickly risen from 3.8% to 22.1% over the past six years.^[6–8] The excellent performance of the organic–inorganic perovskites is governed by their unique properties, such as strong optical absorption, long-range carrier diffusion, high carrier mobility, and the low carrier recombination rates.^[3,9,10]

Owing to combination of inorganic crystalline component associated with PbX₃[−] anions and organic molecule

component associated with MA⁺ cations, MAPbX₃ perovskites are essentially complex materials.^[11,12] At different temperatures, MAPbX₃ exhibits various crystalline structures of orthorhombic, tetragonal, or cubic phases, which determine their optical properties as well as other physics characteristics.^[11,13–18] Previous investigations showed that the structural phase transition from the orthorhombic phase to the tetragonal one and from the tetragonal phase to the cubic one both occur in the temperature range between 80 and 360 K.^[3] Specifically, the tetragonal-to-cubic phase transition occurs within the working temperature range of the perovskite-based solar cells. Furthermore, it has also been demonstrated that the short circuit current and the filling factor both vary dramatically over the orthorhombic-to-tetragonal phase transition. In addition, the power conversion efficiency for solar cells in the tetragonal phase is found to be much higher than that in the other two phases. It has also been reported that the electron mobility of MAPbX₃ perovskites increases significantly with decreasing temperature for different crystalline phases, whereas being sharply decreased at temperature corresponding to the structural phase transition.^[19] Therefore, the study of the temperature-controlled structural phase transitions in the organic–inorganic perovskites is a vital topic for the potential application of these materials, especially for the perovskite-based solar cells.

In addition to temperature, pressure also significantly affects the crystalline structures of the organic–inorganic perovskites.


1. Introduction

In 1978, methylammonium lead halide (MAPbX₃, where MA represents the CH₃NH₃⁺ cation, while X is Cl[−], Br[−], or I[−] anion) was first prepared by Weber using the replacement of Cs⁺ with MA⁺ cation.^[1] Following these materials' initial

F. H. Zhao, Dr. X. Gao, Prof. Y. D. Glinka, Prof. R. Chen
Department of Electrical and Electronic Engineering
Southern University of Science and Technology
Shenzhen, Guangdong 518055, P. R. China
E-mail: chen.r@sustc.edu.cn

Dr. X. Gao, Dr. X. Fang, Prof. Z. P. Wei
State Key Laboratory of High Power Semiconductor Lasers
School of Science
Changchun University of Science and Technology
7089 Wei-Xing Road, Changchun 130022, P. R. China
E-mail: zpweicust@126.com

X. Y. Feng, Prof. Z. B. He
Department of Material Science and Engineering
Shenzhen Key Laboratory of Full Spectral Solar Electricity Generation (FSSEG)
Southern University of Science and Technology
Shenzhen, Guangdong 518055, P. R. China
E-mail: hezb@sustc.edu.cn

 The ORCID identification number(s) for the author(s) of this article can be found under <https://doi.org/10.1002/admi.201800301>.

DOI: 10.1002/admi.201800301

The pressure-induced structural variations of MAPbX_3 perovskites and their optical and electronic properties were studied using the high-pressure single-crystal X-ray diffraction and photoluminescence (PL) techniques.^[20–22] Despite the aforementioned progress is achieved in the study of the structural and optical properties of MAPbX_3 perovskites, the pressure-induced and temperature-induced structural phase transitions and their effect on optical properties of the organic–inorganic perovskites are still not clear. Moreover, it would be important to find out how to control the structural phase of the organic–inorganic perovskites for their better performance in various electronic and optoelectronic devices.

Here we report on the PL study of bare MAPbI_3 perovskite crystal and that being coated with ZnO nanoshell ($\text{MAPbI}_3/\text{ZnO}$). An 10 nm thick ZnO shell was deposited on the surface of MAPbI_3 crystal using the atomic layer deposition (ALD). PL measurements were carried out as a function of the excitation power and temperature to comprehensively monitor the structural phase transitions in the bare and coated MAPbI_3 perovskite crystals. We found that the orthorhombic-to-tetragonal structural phase transition temperature in MAPbI_3 is increased from 135 to 160 K upon coating with ZnO nanoshell. The effect is ascribed to that being induced by the interfacial electric field created by charge separation at $\text{MAPbI}_3/\text{ZnO}$ interface. This study is expected to have a significant impact on the future development of the novel structural-phase-controlled photovoltaic devices that are based on the organic–inorganic perovskites.

2. Results and Discussion

Figure 1b shows the room-temperature PL spectra for the bare MAPbI_3 crystal and that being coated with ZnO shell of 10 nm thickness. Because ZnO nanoshell is extremely thin, the strain induced by it is expected to be negligible. Nevertheless, ZnO nanoshell significantly affects PL properties of MAPbI_3 crystal, as appeared in a pronounced blue-shift (20 meV) of the PL band. Grancini et al.^[23] reported on a blue shift of PL emission at the edge of a MAPbI_3 crystal as compared from a region away from the edge. However, we selected the center of samples for the measurements both for bare MAPbI_3 and $\text{MAPbI}_3/\text{ZnO}$, this reason could be ruled out. The latter tendency suggests that the near-surface region completely determines PL properties of MAPbI_3 crystals coated with ZnO nanoshell, despite the light penetration depth in MAPbI_3 is known to be 1.0 μm .^[24] This unusual behavior points out that the electronic transitions taking place in the near-surface region dominate over those occurring in the crystal bulk. We associate this behavior with the formation of ZnO surface quantum well (SQW).^[25] Correspondingly, ZnO SQW is confined on one side by the vacuum potential and on the other side by the potential associated with MAPbI_3 . Because the band offset between ZnO and MAPbI_3 is known to be 0.26 eV,^[26] ZnO SQW can actually be formed, significantly affecting PL properties of MAPbI_3 through the interfacial electric field created due to charge separation at $\text{MAPbI}_3/\text{ZnO}$ interface (Figure 2a).

Using Gaussian profiles to fit the emission bands, the aforementioned blue-shift observed for $\text{MAPbI}_3/\text{ZnO}$ at 300 K has

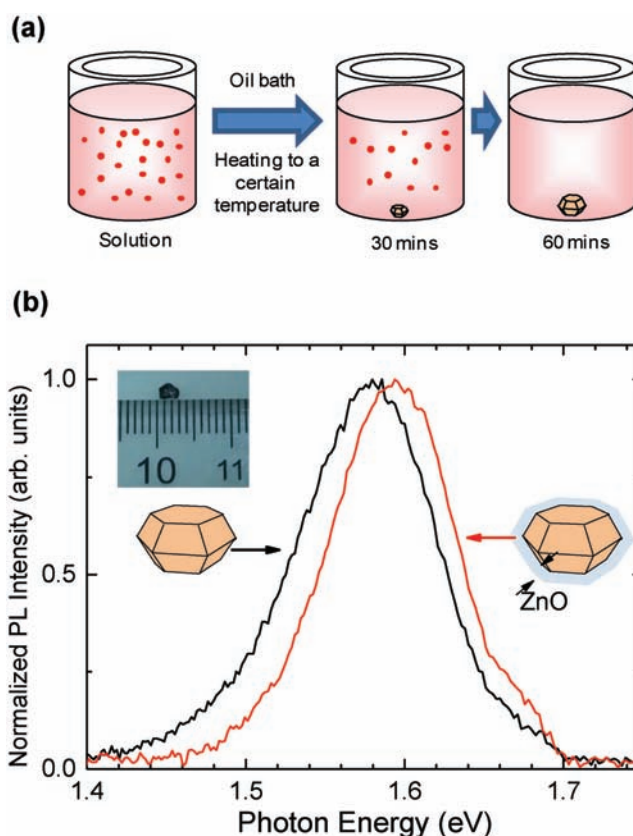


Figure 1. a) Schematic presentation of the MAPbI_3 crystal synthesis using the inverse temperature crystallization technique. b) PL spectra of MAPbI_3 and $\text{MAPbI}_3/\text{ZnO}$ measured at 300 K with power density of 8.0 W cm^{-2} , as indicated by the corresponding color arrows and crystal images. Inset shows the photograph of MAPbI_3 single crystal used in this study.

been suggested to originate from the quenching of the lower-energy PL band by the interfacial electric field. This statement takes into account that the broad PL band observed for the bare MAPbI_3 crystal consists of two bands, while the lower-energy one can be quenched when the interfacial electric field is developed. We associate these two bands with the radiative recombination of free excitons (FX) (the lower-energy PL band) and the band-to-band radiative electron–hole recombination (the higher-energy PL band). Consequently, PL quenching can be attributed to FX dissociation induced by the interfacial electric field, the process which is well known for the stacked photovoltaic and organic solar cells,^[27,28] and which is expected to occur at thermal energies comparable to the FX binding energy.^[27]

The effect becomes more prominent with increasing temperature, as appeared in PL spectra measured at 340 K, when thermal energy is slightly above the FX binding energy (Figure 3). The integrated PL intensity for both crystals increases superlinearly with laser power (slope in the log–log plot 1.5) (Figure 3a, inset), demonstrating a typical behavior for MAPbI_3 perovskites.^[29] The reason for this superlinearity might be due to the combination of several processes, such as two-step one-photon or two-photon excitations followed by carrier multiplication, impact ionization, and Auger recombination.^[30,31] Despite the peak energy of the PL band for both

crystals remains almost unchanged with increasing laser power, PL bandwidth in bare MAPbI₃ is remarkably larger as compared to MAPbI₃/ZnO being additionally increased with increasing laser power (Figure 3b, inset). The latter behavior is well consistent with the FX nature of the lower-energy side of the PL band and confirms that its broadening is due to collisions among FX or with free-carriers when the laser power (photoexcited carrier density) becomes high enough.^[32] It is clear now that if the interfacial electric field suppresses the FX dynamics in MAPbI₃/ZnO crystal, the lower-energy side of the PL band is getting quenched. Consequently, the resulting PL band becomes much narrower, although remaining to be slightly asymmetric. This dynamics appears as a blue-shift of the PL band as a whole. Figure 3 clearly shows that the subtraction of the PL band observed for MAPbI₃ from that observed for MAPbI₃/ZnO allows for recognizing the partial PL intensity, which was suppressed and enhanced in the bare MAPbI₃ crystal upon coating with ZnO nanoshell. This dynamics points out that the interfacial electric field redistributes the FX effect toward the free-carrier one, thus increasing the efficiency of charge transfers across the material.

PL spectra measured for MAPbI₃ and MAPbI₃/ZnO crystals become more complicated with decreasing temperature at which the orthorhombic-to-tetragonal phase transition occurs (Figure 4). One can recognize totally three PL bands that are peaked in the spectral range where the radiative recombination of FX in MAPbI₃ can usually be observed (denoted in Figure 4 as P0, P1, and P2). For the orthorhombic structural phase dominating at 10 K, light emission appears through the P0 and

P1 bands (Figures 4 and 5), which were assigned to the radiative recombination of carrier trapped by the structural defects [Frenkel defects (FD) of 10¹⁷ cm⁻³ density]^[33,34] and the radiative recombination of FX, respectively.

The P0 band becomes significantly enhanced for MAPbI₃/ZnO, indicating that ZnO nanoshell induces an additional concentration of FD at MAPbI₃/ZnO interface. The integrated intensity of the P0 band for both MAPbI₃ and MAPbI₃/ZnO crystals increases linearly with increasing laser power followed by saturation at higher powers (Figure 5, inset). This behavior can be described in the frame of the first-order trapping kinetics.^[35] Specifically, because FD act as the electron traps, the P0 band intensity is proportional to the density of electrons trapped by FD ($I_{PL} \propto n^*$), which in turn is determined by the trap density n_t and the free-electron density n as

$$n^* = n_t [1 - \exp(-\sigma \delta_p n)] \quad (1)$$

where σ and δ_p are the trapping cross-sections and the characteristic interaction length (light penetration depth), respectively. To fit the measured power dependences of the PL integrated intensity, one can reasonably assume that the density of photoexcited free-electrons is proportional to the applied laser power density ($I_L \propto n$). Then, Equation (1) can be modified to

$$I_{PL} = A [1 - \exp(-BI_L)] \quad (2)$$

where A and B can be used as fitting parameters. The result of the fit shows good agreement with the first-order trapping

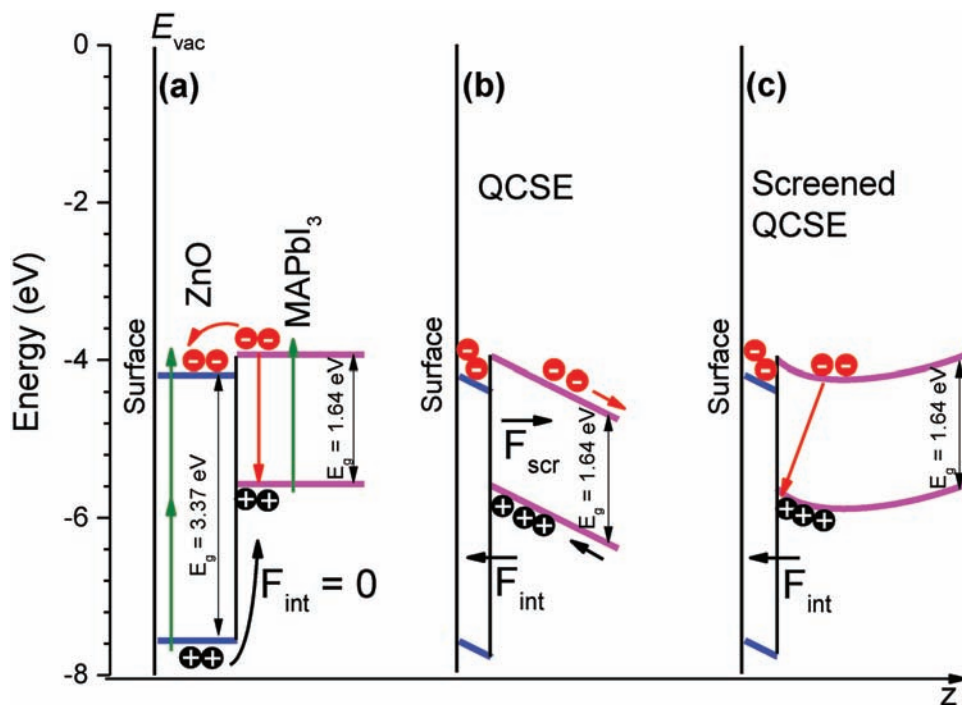


Figure 2. a) Energy band diagram of MAPbI₃/ZnO heterointerface. The charge separation at the heterointerface after carrier excitation with the one-photon and two-photon processes is shown. b) The interfacial-electric-field-induced tilting of the energy band structure, which is responsible for conventional QCSE. The interfacial-electric-field-induced charge separation in the MAPbI₃ bulk, which forms the screening electric field \vec{F}_{scr} , is shown. c) The energy band diagram at equilibrium when \vec{F}_{int} is completely screened by \vec{F}_{scr} at some specific distance from the interface (screened QCSE). The variation of the band structure of MAPbI₃ along z-axis is shown in accordance with the numerically simulated result obtained using Equation (6).

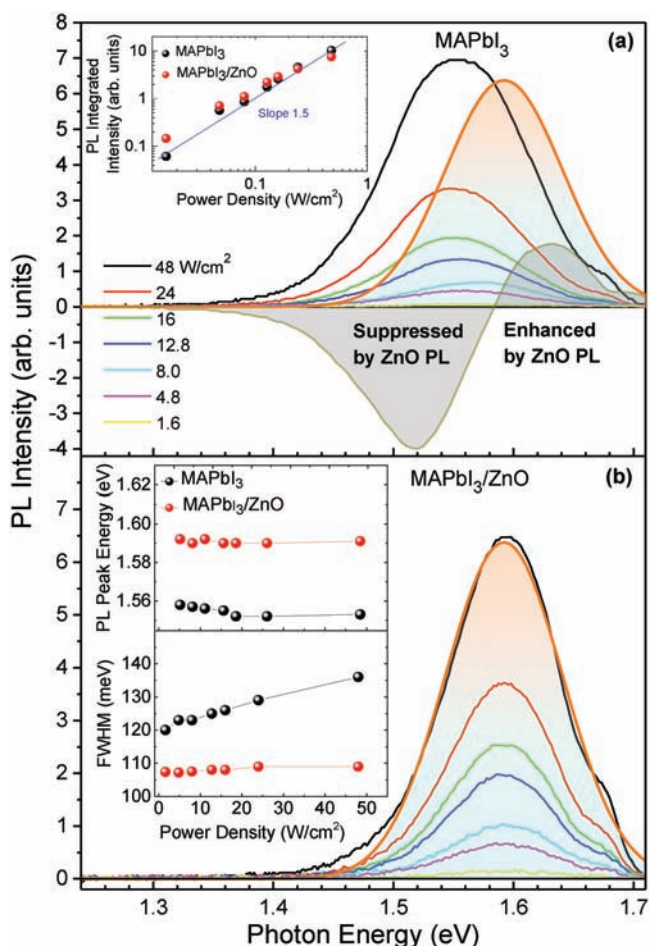


Figure 3. a,b) PL spectra of MAPbI₃ and MAPbI₃/ZnO measured at 340 K with different power densities, as indicated by the corresponding colors. Insets show the power dependences of the integrated PL intensity, the PL peak energy, and the PL band FWHM. The filled Gaussian profile (orange) for PL spectrum measured with 48.0 W cm⁻² power density for MAPbI₃/ZnO is shown in both (a) and (b). The difference between the Gaussian profile of PL band measured for MAPbI₃/ZnO and PL spectrum measured for MAPbI₃ is shown in (a) as gray-filled area, which indicates the partial PL intensity that was suppressed (negative) and enhanced (positive) by ZnO nanoshell.

kinetics (Figure 5, inset). The P0 band gradually blue-shifts with increasing laser power (Figure 5, inset). This behavior indicates that the photoexcited carriers occupy the more energetic FD states with increasing photoexcited carrier density.

The integrated intensity of the P1 band resulting from FX radiative recombination for the bare MAPbI₃ crystal increases superlinearly (slope in the log–log plot 1.5) with increasing laser power (Figure 5a, inset), similarly to that observed for the high-temperature measurements (Figure 3a, inset). By contrast, the P1 band integrated intensity for MAPbI₃/ZnO crystal demonstrates a similar superlinear rising trend on the initial stage followed by a more than quadratic power dependence for higher powers (slope in the log–log plot 2.4). The quadratic-type power dependence clearly indicates that the two-photon PL excitation regime dominates in MAPbI₃/ZnO for higher laser powers. We associate the latter behavior with two-photon

absorption in ZnO nanoshell. By contrast, the one-photon carrier excitation regime occurs in both crystals due to one-photon absorption in MAPbI₃ (Figure 2a).

For the lowest excitation powers applied, the P1 band for MAPbI₃/ZnO crystal shows an initial red-shift (36 meV) with respect to the position of the P1 band for the bare MAPbI₃ crystal. However, the P1 band position for MAPbI₃/ZnO almost completely recovers to that for MAPbI₃ (blue-shift) with increasing laser power (Figure 5). We note here that despite the blue-shifts for P0 and P1 bands with increasing laser power demonstrate similar trends (Figure 5, inset), they have different nature. To explain the blue-shift of the P1 band, we consider the possible confinement-induced mechanisms which could potentially contribute to the observed red and blue shifts of the P1 band resulting from the FX radiative recombination.

The first mechanism can be associated with the upward shift of electronic levels with decreasing ZnO SQW width due to the quantum confinement effect^[36]

$$E_{PL} = E_g + (1/m_e + 1/m_h) \hbar^2 \pi^2 / 2L_w^2 \quad (3)$$

where E_g is the ZnO bandgap energy, m_e and m_h are the in-plane electron and hole effective masses, and L_w is the ZnO SQW width. However, because the ZnO SQW width is unchanged and because quantum confinement mainly affects the photoexcited carrier dynamics in ZnO SQW, the effect of this mechanism on PL from MAPbI₃ seems to be negligible. Another mechanism is known as the quantum-confined Stark effect (QCSE),^[37–39] which is caused by the strong interfacial electric field originating from charge separation between photoexcited electrons and holes at MAPbI₃/ZnO interface (Figure 2b). In general, this mechanism can affect the photoexcited carrier dynamics in both ZnO and MAPbI₃. We consider first the conventional QCSE in ZnO SQW, which is known to provide the following energy of the PL peak^[37]

$$E_{PL} = E_g - p\bar{F}_{int} + \beta\bar{F}_{int}^2 \quad (4)$$

where p is a permanent dipole moment of bound electron–hole pairs in ZnO SQW, \bar{F}_{int} is the interfacial electric field defined as $\bar{F}_{int} = -\delta\phi_{int}/L_{int}$ with $\delta\phi_{int}$ being the change in the electrostatic potential at MAPbI₃/ZnO interface of width L_{int} and is a polarizability of electrons and holes.^[39] The latter quantity characterizes an extension of electron and hole ground state wave functions in the direction along the sample normal (z-axis). QCSE is hence responsible for a red-shift of the PL band originating from radiative electron–hole recombination in ZnO SQW [second term in Equation (4)], which we actually do not monitor in the current study. Alternatively, because the interfacial electric field pulls the electron and hole wave functions apart, the electrons/hole polarizability [third term in Equation (4)] is responsible for the blue-shift. However, for low and moderate carrier densities photoexcited, the latter effect is known to be much weaker as compared to that originating from the dipole-field interaction [second term in Equation (4)]. Therefore, this effect is expected to manifest itself only at high photoexcited carrier densities, which we believe have not been reached in our experiments. Now we apply QCSE to the aforementioned indirect excitons, the PL trace of which has also not

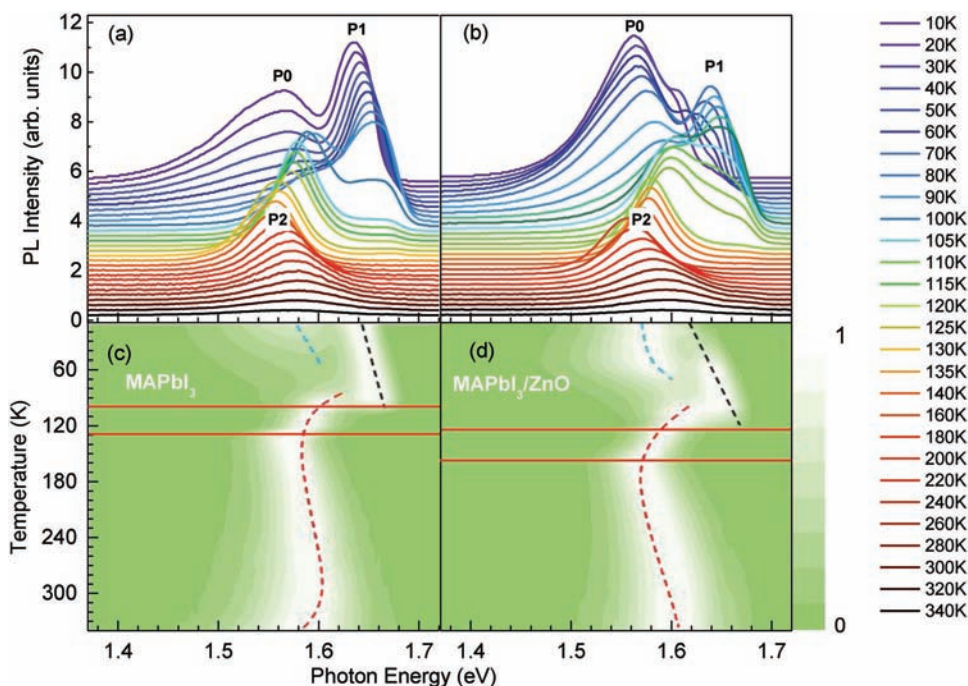


Figure 4. The PL spectra of a) MAPbI₃ and b) MAPbI₃/ZnO measured with power density of 8.0 W cm⁻² and at different temperatures, as indicated by the corresponding colors. c,d) The corresponding contour plots of the normalized PL spectra. The dashed lines show the general tendencies of the PL peak shift. The horizontal red lines indicate the intermediate temperature range where both phases coexist.

been observed in our experiments. Nevertheless, in this case QCSE should demonstrate the red shift in assumption that p in Equation (4) is a permanent dipole moment of indirect excitons at MAPbI₃/ZnO interface.

The mentioned confinement-induced mechanisms completely govern the carrier dynamics in different-type QWs.^[36–39] However, they cannot explain the observed for MAPbI₃/ZnO crystal blue-shift of the P1 band with increasing carrier density. This circumstance suggests that the observed blue-shift is unique and a more distinct model should be developed to explain it. Specifically, this model should take into account the effect of the interfacial electric field at MAPbI₃/ZnO interface on photoexcited carriers in the near-interface region of MAPbI₃ crystal and the corresponding screening effect. Because the cw regime of carrier excitation with photon energy of 1.69 eV is used in our experiments, the excess electron energy in MAPbI₃ is 50 meV. The cooling of electrons and holes allows for their trapping by FD and binding them to create FX. However, because of the continuous photoexcitation of carriers, FX and free-carriers coexist in the crystal under certain equilibrium as long as the photoexcitation is applied. The direct recombination of hot free electrons and holes is not allowed due to the energy-momentum conservation law,^[36] although it can occur at higher temperatures and for higher carrier densities through the collision-induced mechanism. Consequently, we reasonably assume that the interfacial electric field at MAPbI₃/ZnO interface is getting completely screened by free electrons photoexcited in the near-interface region of MAPbI₃ at some specific distance from the interface. The QCSE mechanism for FX in MAPbI₃ then can be modified to

$$E_{\text{PL}} = E_g - p_i \bar{F}_{\text{int}}^{\text{scr}} \quad (5)$$

where p_i is an induced dipole moment of the pairs of electrons and holes separated by \bar{F}_{int} in MAPbI₃, $\bar{F}_{\text{int}}^{\text{scr}}$ is a screened interfacial electric field defined as $\bar{F}_{\text{int}}^{\text{scr}} = -\delta\phi_{\text{scr}}(z)k_{\text{TF}}$, where k_{TF} is the Thomas–Fermi wavevector and $\phi_{\text{scr}}(z)$ is the screened Coulomb potential.^[40] The screened interfacial electric field can schematically be presented as $\bar{F}_{\text{int}}^{\text{scr}} = \bar{F}_{\text{int}} - \bar{F}_{\text{scr}}$, where \bar{F}_{scr} is the screening electric field in MAPbI₃ (Figure 2). Specifically, \bar{F}_{int} initiates a band structure tilting in MAPbI₃ which leads to moving of photoexcited free electrons away from the interface inward toward the bulk.^[41] Alternatively, the photoexcited free holes accumulate in MAPbI₃ in the close proximity to the interface. The resulting charge separation can be associated with \bar{F}_{scr} , which acts oppositely to \bar{F}_{int} until completely screens it at the distance that is known as the Thomas–Fermi screening length k_{TF}^{-1} , which for free-electron gas can be defined as $k_{\text{TF}}^2 \approx 4m_q q^2 \hbar^{-2} n^{1/3}$ with q , m_q , and n being the electron charge, the effective mass, and the electron density, respectively.^[40] The explicit form of $\phi_{\text{scr}}(z)$ can be obtained by solving the corresponding screened Poisson's equation $[\nabla^2 - k_{\text{TF}}^2] \delta\phi_{\text{scr}}(z) = -\rho(z)/\epsilon_0$, where $\rho(z)$ is the charge density and ϵ_0 is the vacuum permittivity, so that $\phi_{\text{scr}}(z) = q \exp(-k_{\text{TF}} z)/z$,^[42] where z is the distance from the interface inward toward the MAPbI₃ bulk. Finally, Equation (5) can be rewritten as

$$E_{\text{PL}} = E_g + \frac{p_i q}{z k_{\text{TF}}^{-1}} e^{-k_{\text{TF}} z} \quad (6)$$

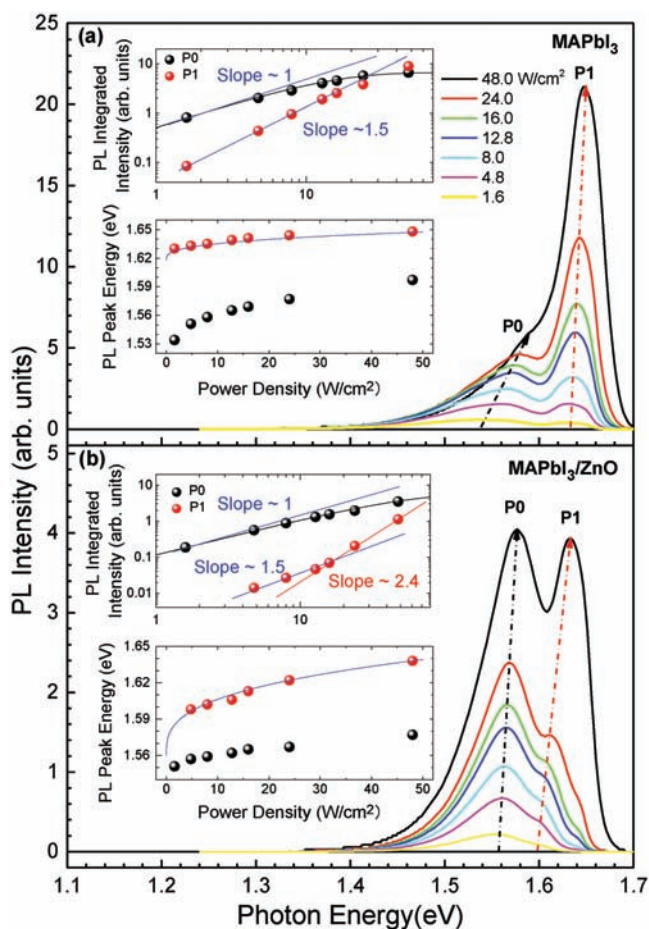


Figure 5. The PL spectra of a) MAPbI_3 and b) $\text{MAPbI}_3/\text{ZnO}$ measured at 10 K with different excitation powers, as indicated by the corresponding colors. Two PL peaks are denoted as P0 and P1. Dashed lines indicate the shift of P0 and P1 with increasing laser power. Insets show the excitation power dependences of the PL integrated intensities and the PL peak energies for P0 and P1, as indicated by the corresponding colors. The fits to the data are shown (see text).

This equation presents the screened QCSE and has a simple physical meaning that \vec{E}_{int} tilts the interface electronic structure (Figure 2) with its further recovering when the distance from the interface inward toward the MAPbI_3 bulk exceeds the Thomas–Fermi screening length. It is obvious that if $z < k_{\text{TF}}^{-1}$, the PL peak associated with FX experiences a red-shift in full agreement with the conventional QCSE. This is a reason why the P1 band in $\text{MAPbI}_3/\text{ZnO}$ is red-shifted with respect to that in bare MAPbI_3 when lowest laser power is applied. However, once the critical condition ($z = k_{\text{TF}}^{-1}$) is reached with increasing laser power, that is, with increasing $n(I_L - n)$, a blue-shift can be observed because Equation (6) yields

$$E_{\text{PL}} = E_{\text{g}} + An^{1/3} \propto E_{\text{g}} + AI_L^{1/3} \quad (7)$$

where $A \approx \frac{4}{3} p_i m_q q^3 \hbar^{-2}$ can be used as a fitting parameter. The result of the fit shows good agreement with the proposed model (Figure 5, inset). We note that this model can also be applied for the bare MAPbI_3 crystal in assumption that the depletion electric field induced by surface defects acts in a similar way as the

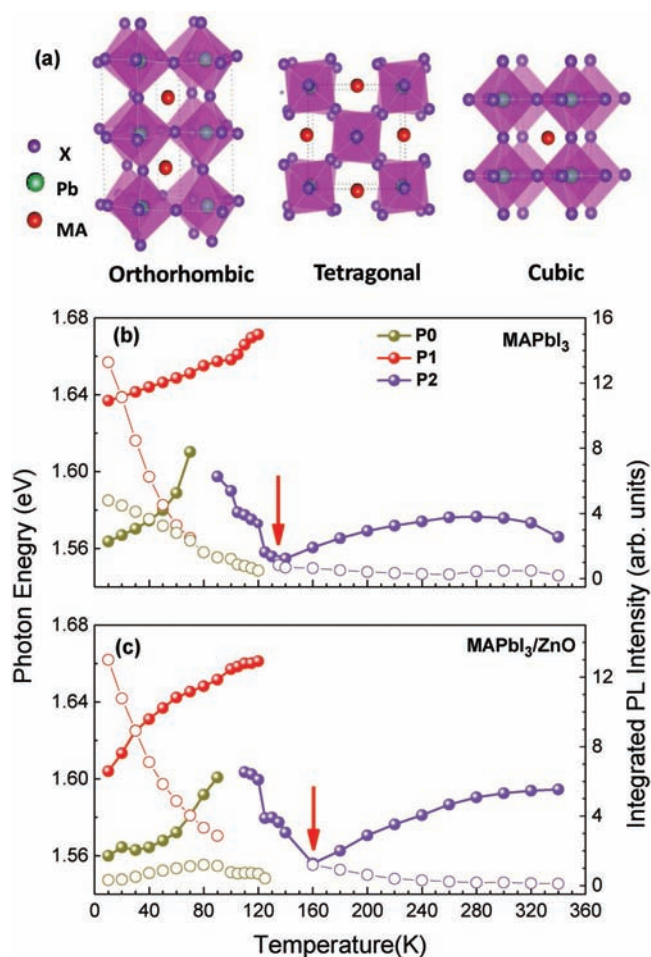


Figure 6. a) Crystal structure of different perovskites phases, as indicated. b,c) Temperature dependences of the PL peak position (filled circles) and the integrated PL intensity (open circles) for three PL bands, as indicated by the corresponding colors for MAPbI_3 and $\text{MAPbI}_3/\text{ZnO}$, respectively. Vertical red arrows in (b) and (c) show the specific temperatures at which the orthorhombic-to-tetragonal structural phase transition occurs.

interfacial electric field at $\text{MAPbI}_3/\text{ZnO}$ interface. This assumption well agrees with the much smaller blue-shift observed for the bare MAPbI_3 crystal (Figure 5, inset).

The FD-related PL band (P0) completely disappears with increasing temperature at which the orthorhombic-to-tetragonal phase transition occurs (Figures 4 and 6). This fact indicates that the crystalline structure becomes more perfect for the tetragonal phase. Figure 7 shows the normalized PL spectra measured within the intermediate temperature range where both structural phases coexist. One can see that additionally to the P1 band, there is the PL band associated with the tetragonal phase (P2). These temperature-dependent measurements clearly show that a decrease of the P1 band intensity is accompanied by an increase in the intensity of the P2 band. Moreover, the P2 band gradually red-shifts with increasing temperature within the intermediate temperature range (Figures 6 and 7). However, the spectral rearrangement for $\text{MAPbI}_3/\text{ZnO}$ occurs at higher temperatures as compared to MAPbI_3 . This behavior indicates the shift of the entire intermediate temperature range

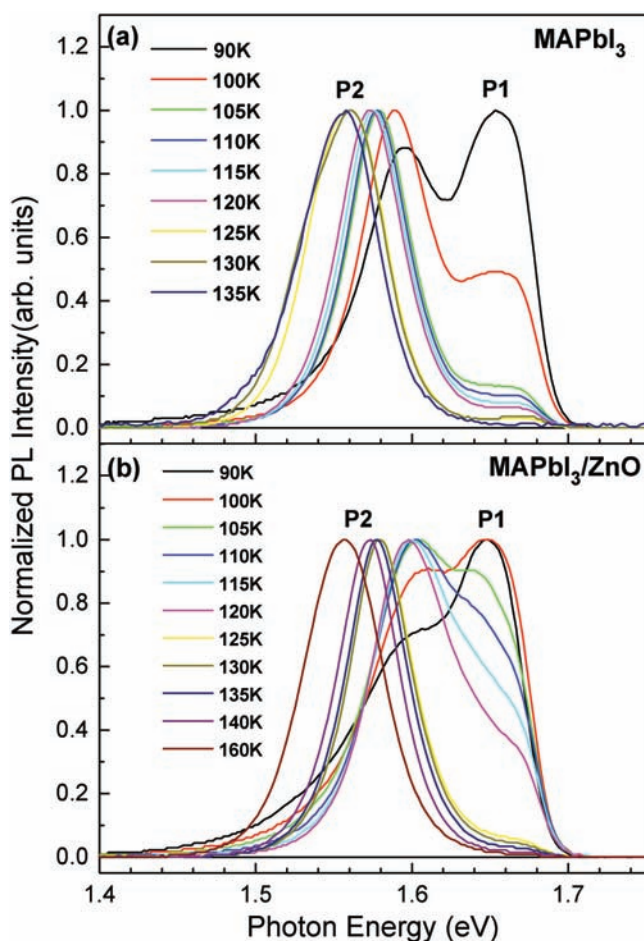


Figure 7. The normalized PL spectra of a) MAPbI₃ and b) MAPbI₃/ZnO measured with power density of 8.0 W cm⁻² and at different temperatures, as indicated by the corresponding colors. The groups of PL peaks associated with the orthorhombic and tetragonal structural phases are denoted as P1 and P2, respectively.

of the orthorhombic-to-tetragonal phase transition toward the higher temperatures (Figures 4 and 7). However, the effect can be seen with a higher level of precision by analyzing the position of PL peaks within the whole temperature range applied in the current study (Figure 6). Correspondingly, the orthorhombic-to-tetragonal structural phase transition temperature in MAPbI₃ is increased from 135 to 160 K upon coating with ZnO nanoshell. We explain this effect as being caused by an atomic rearrangement in the near-surface area induced by the interfacial electric field arising due to charge separation at MAPbI₃/ZnO interface.^[43] For the phase transition temperature from tetragonal to orthorhombic of bare MAPbI₃, it has been reported to be in the range 140–170 K and appear to depend strongly on the perovskites processing route and grain size.^[44,45]

Another remarkable feature is the blue-shift of the P0 and P1 bands with increasing temperature in the range preceding the orthorhombic-to-tetragonal phase transition (Figure 6). This blue-shift is accompanied by the significant weakening of the corresponding PL bands. The intensity decrease can be associated with an increase of the nonradiative recombination rate when approaching to the phase transition temperature. The

blue shift of the P0 band with increasing temperature is believed to have the same nature as that observed with increasing laser power density (Figure 5, inset), thus indicating that more energetic traps are involved into the FD-related light emission with increasing temperature. Meanwhile, the blue shift of the FX-related emission band is opposite to that the Varshni's relation usually predicts.^[46] Moreover, this blue shift appears for the both structural phases (P1 and P2 bands, respectively), whereas the behavior sharply switches to the red shift at temperatures corresponding to the structural phase transitions (Figure 6). This dynamics with increasing temperature is totally consistent with that observed with decreasing temperature for the electron mobility of MAPbX₃ perovskites.^[19] This common tendency can be understood in the frame of the model that takes into account Bose–Einstein statistical factors for phonon emission and absorption by hot carriers.^[47,48] Accordingly, the bandgap of semiconductors varies with temperature as

$$E_g(T) = a - b \left(1 + \frac{2}{e^{\theta/T} - 1} \right) = a - b [\coth(\theta/2T)] \quad (8)$$

where a and b are fitting parameters and θ represents the mean temperature of the phonons taking part in the scattering process with carriers.^[48] It is clear that $E_g(T)$ can show either a decrease (red shift) or an increase (blue shift) depending on whether derivative d/dT is positive (phonon emission) or negative (phonon absorption), respectively. Consequently, the blue shift of the P1 and P2 band observed for the orthorhombic and tetragonal phases, respectively, points out that the hot (nonequilibrium) carrier dynamics completely governs the PL properties of MAPbI₃ and MAPbI₃/ZnO perovskites with increasing temperature. This conclusion is well consistent with the recent observation of long-lived nonequilibrium carriers resulting from the blocking of phonon propagation, which is caused by an ultralow thermal conductivity of the organic-inorganic hybrid perovskites.^[49] It should be especially stressed that because the longitudinal optical (LO)-phonon emission is the dominant scattering mechanism limiting charge-carrier mobility,^[50] nonequilibrium carriers that reabsorb LO-phonons should hence reveal the enhanced electron mobility.^[19]

In the intermediate temperature range, the P2 band shows a red shift, indicating that the phonon emission process dominates over the phonon absorption one, thus pointing to the efficient carrier cooling. For the same reason, the red shift becomes more prominent for the P2 band when approaching to the tetragonal-to-cubic phase transition temperature (Figure 6). The comparison of this dynamics with that observed for the electron mobility^[19] allowed us to conclude that the high electron mobility and long-range electron diffusion of MAPbX₃ perovskites are likely associated with the hot (nonequilibrium) carrier dynamics including the hot-phonon bottleneck effect,^[49] which results from the ultralow thermal conductivity between organic and inorganic crystal-line components.

Now we analyze the laser-power-dependent dynamics of the P2 band which is associated with radiative recombination of FX residing in the tetragonal structural phase (Figure 8). The remarkable feature is that the power dependence of the PL band integrated intensity still follows the

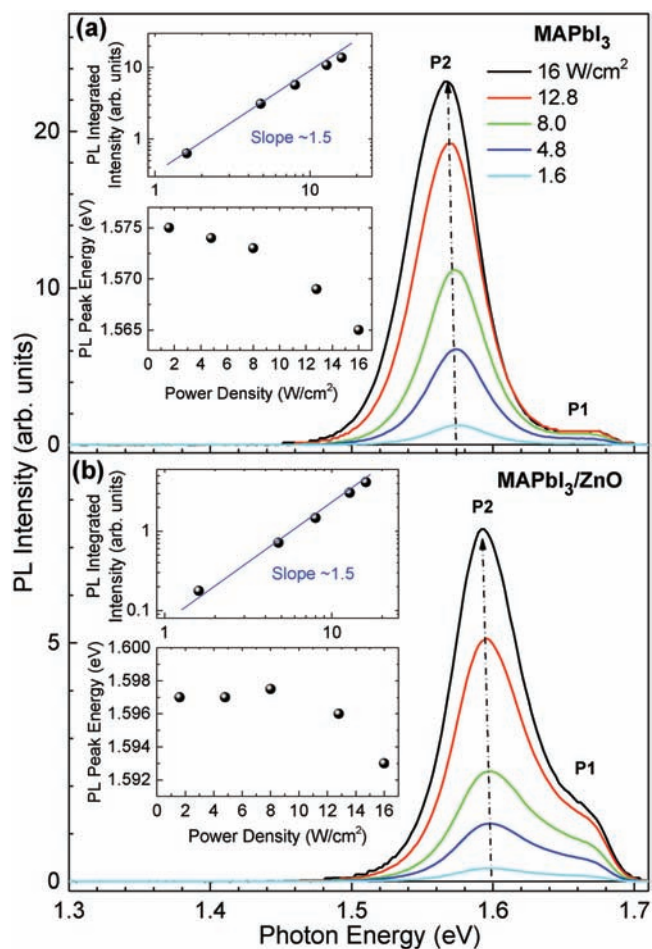


Figure 8. PL spectra of a) MAPbI₃ and b) MAPbI₃/ZnO measured at 120 K with different excitation powers, as indicated by the corresponding colors. Insets show the corresponding power dependences of the PL integrated intensities and peak positions.

power law with index 1.5, indicating that this behavior is common for all structural phases of MAPbI₃ perovskite. The initial blue-shift of the P2 band in MAPbI₃/ZnO with respect to that in MAPbI₃ is due to the shift of the intermediate temperature range toward the higher temperature, as discussed above (Figure 7). As laser power increases, the P2 band shows a small red-shift for both samples. This fact together with a similar P2 band bandwidth indicates that the power-dependent dynamics in this case reflects the laser heating effect rather than the screened QCSE. Specifically, the laser heating effect enhances the phonon emission rate ($d\epsilon/dT$ is positive) and hence introduces the bandgap decrease and the corresponding red-shift in accordance with Equation (8).^[47,48] The screened QCSE in this case is masked by strong Fröhlich interaction with LO-phonons.^[49,50]

The latter statement can be proved by analyzing the temperature dependence of the PL bandwidth, which can be fitted using a phenomenological approximation for phonon-induced broadening^[50,51]

$$\gamma = \Gamma_0 + \gamma_{ac}T + \gamma_{LO} / [(E_{LO}/k_B T) - 1] \quad (9)$$

where Γ_0 is inhomogeneous broadening, γ_{ac} is electron-acoustic-phonon coupling strength, γ_{LO} represents the strength of electron-LO-phonon coupling, and E_{LO} is the LO-phonon energy. The fitting parameters obtained for the orthorhombic and tetragonal phases of MAPbI₃ and MAPbI₃/ZnO crystals are listed in Figure 9 and are well consistent with those previously reported.^[50] Accordingly, the electron-acoustic-phonon scattering remarkably contributes exclusively into the low-temperature orthorhombic phase dynamics while it is negligible for the tetragonal phase dominating at higher temperatures. Alternatively, the electron-LO-phonon coupling in the tetragonal phase is much stronger than that in the orthorhombic one. This conclusion is in good agreement with previous reports.^[50]

3. Conclusion

In summary, we have evidenced that ZnO nanoshell significantly affects the PL properties of MAPbI₃ crystal through the interfacial electric field arising at the heterointerface due to efficient charge separation. The PL properties of the coated perovskite crystal are mainly governed by the closeness to the surface area. At the working temperature of perovskite-based solar cells, the interfacial electric field significantly suppresses the PL band associated with FX dynamics in MAPbI₃/ZnO, thus enhancing the PL band associated with the free-carrier recombination. The resulting increase of the free-carrier density is expected to enhance the charge transfer across MAPbI₃ perovskites and it could be important for the applications in photovoltaic devices based on perovskites. For the low-temperature structural phase (orthorhombic), we have observed the interfacial-field-induced screened QCSE. However, this effect becomes unobservable for the high-temperature phase (tetragonal) being masked by the strong Fröhlich interaction with LO-phonons and the laser heating effect. We also have provided an additional proof that the high electron mobility of MAPbX₃ perovskites is likely associated with the hot (nonequilibrium) carrier dynamics, which includes the hot-phonon bottleneck effect resulting from the ultralow thermal conductivity between organic and inorganic crystalline components. Finally, we have observed the interfacial-field-induced increase of the orthorhombic-to-tetragonal structural phase transition temperature in MAPbI₃ from 135 to 160 K upon coating with ZnO nanoshell. This kind of effect is believed to be common for the variety of perovskite materials and affects the potential applications of MAPbI₃ perovskites in the structural-phase-controlled optoelectronic and photovoltaic devices.

4. Experimental Section

Chemicals and Reagents: Lead iodide (99.999% trace metal basis) and γ -butyrolactone (GBL, 99%) were purchased from Sigma-Aldrich. Methylammonium iodide (MAI) was purchased from Dyesol Limited.

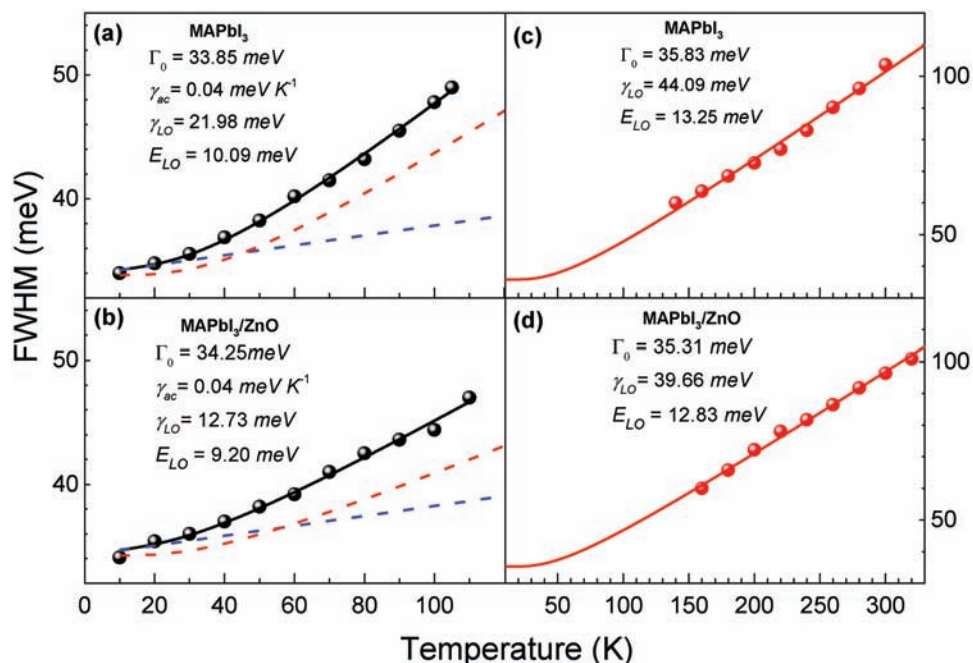


Figure 9. Temperature dependences of FWHM of the P1 and P2 bands corresponding to the a,b) orthorhombic and c,d) tetragonal phases, respectively, for MAPbI₃ and MAPbI₃/ZnO, as indicated. Black and red solid lines show the best fits to the data obtained using Equation (8). The corresponding inhomogeneous broadening (Γ_0), electron–acoustic-phonon coupling strengths (γ_{ac}), electron–LO-phonon coupling strengths (γ_{LO}) and LO-phonon energies (E_{LO}) used for fits are listed for each of the dependences. The red dashed line indicates the contribution from the LO-phonon only, and the blue dashed line shows the contribution from the acoustic-phonon scattering alone. The inhomogeneous broadening was included in both cases.

(Australia). Zn(C₂H₅)₂ (DEZn) and oxygen plasma were supplied by Guangfu Chemical Reagent Factory in Tianjin, China. All reagents were used without any further purification.

Synthesis of MAPbI₃ and MAPbI₃/ZnO Samples: The detailed procedure of synthesis was described in the literature.^[24] First, the solution containing PbI₂ and MAI was prepared in GBL with heating up to 60 °C. Then solution was filtered using poly tetra fluoroethylene (PTFE) filter with 0.2 μm pore size. The filtrates were placed in a beaker and the beaker was kept in an oil bath at 110 °C (Figure 1a). The crystals in this study were grown for 3 h. MAPbI₃/ZnO sample was synthesized by ALD system (Ensure Nanotech-LabNano-PE). DEZn (Zn(C₂H₅)₂) and oxygen plasma were used as precursors, high purity Ar was used as the purging and carrier gas. In the deposition processes, oxygen plasma and DEZn were introduced into the growth chamber separately. Ar purge was introduced after precursors pulse to remove the residues and byproducts. Gas flow rate can be controlled by mass flow controller. And the typical plasma enhanced atomic layer deposition (PEALD) ZnO growth cycle was composed of 5 sccm of oxygen plasma, 5 sccm of Ar purging, and 40 ms of DEZ exposure. The sample was grown at room temperature and the total growth cycles were 100 cycles.

Measurement and Characterization: PL measurements were performed with a HORIBA iHR550 spectrograph, and the PL spectra were detected by an InGaAs detector. A 655 nm semiconductor diode laser was used as the excitation source. The temperature of the samples was controlled between 10 and 340 K by a closed-cycle helium cryostat (Janis CCS-150). The excitation power of 627 mW and the spot diameter of the laser on the samples of about 100 μm were used during temperature dependent PL spectra measurement.

Acknowledgements

This work was supported by the Natural Science Foundation of China (NSFC Grant Nos. 11574130, 11404161, 61307045, 61404009, 61474010, 61574022, and 61504012), Shenzhen Science and Technology

Innovation Committee (Projects Nos. KQJSCX20170726145748464, JCYJ20150930160634263, and KQTD2015071710313656), the Shenzhen Key Laboratory Project (Grant No. ZDSYS201602261933302), the Foundation of State Key Laboratory of High Power Semiconductor Lasers, the Developing Project of Science and Technology of Jilin Province (Grant Nos. 20160519007JH and 20160520117JH), and the Project of Education Department of Jilin Province [Grant No. 2015(70)]. R.C. acknowledges the support from national 1000 plan for young talents.

Conflict of Interest

The authors declare no conflict of interest.

Keywords

interfacial field, perovskite crystals, phase transition, quantum-confined Stark effect, surface quantum well

Received: February 22, 2018
Revised: March 17, 2018
Published online: May 2, 2018

- [1] D. Weber, *Z. Naturforsch., B: J. Chem. Sci.* **1978**, *33*, 1443.
- [2] J. H. Heo, M. H. Lee, H. J. Han, B. R. Patil, J. S. Yu, S. H. Im, *J. Mater. Chem. A* **2016**, *4*, 1572.
- [3] H. Zhang, X. Qiao, Y. Shen, T. Moehl, S. M. Zakeeruddin, M. Grätzel, M. Wang, *J. Mater. Chem. A* **2015**, *3*, 11762.
- [4] G. Li, Z.-K. Tan, D. Di, M. L. Lai, L. Jiang, J. H.-W. Lim, R. H. Friend, N. C. Greenham, *Nano Lett.* **2015**, *15*, 2640.

- [5] J. M. Ball, M. M. Lee, A. Hey, H. J. Snaith, *Energy Environ. Sci.* **2013**, 6, 1739.
- [6] A. Kojima, K. Teshima, Y. Shirai, T. Miyasaka, *J. Am. Chem. Soc.* **2009**, 131, 6050.
- [7] Y. Zhao, K. Zhu, *J. Phys. Chem. C* **2014**, 118, 9412.
- [8] S. Tombe, G. Adam, H. Heilbrunner, D. H. Apaydin, C. Ulbricht, N. S. Sariciftci, C. J. Arendse, E. Iwuoha, M. C. Scharber, *J. Mater. Chem. C* **2017**, 5, 1714.
- [9] C. Quarti, E. Mosconi, J. M. Ball, V. D'Innocenzo, C. Tao, S. Pathak, H. J. Snaith, A. Petrozza, F. De Angelis, *Energy Environ. Sci.* **2016**, 9, 155.
- [10] G. Xing, N. Mathews, S. Sun, S. S. Lim, Y. M. Lam, M. Grätzel, S. Mhaisalkar, T. C. Sum, *Science* **2013**, 342, 344.
- [11] T. Baikie, Y. Fang, J. M. Kadro, M. Schreyer, F. Wei, S. G. Mhaisalkar, M. Graetzel, T. J. White, *J. Mater. Chem. A* **2013**, 1, 5628.
- [12] L. Dimesso, M. Dimamay, M. Hamburger, W. Jaegermann, *Chem. Mater.* **2014**, 26, 6762.
- [13] K. Wu, A. Bera, C. Ma, Y. Du, Y. Yang, L. Li, T. Wu, *Phys. Chem. Chem. Phys.* **2014**, 16, 22476.
- [14] V. D'Innocenzo, G. Grancini, M. J. Alcocer, A. R. S. Kandada, S. D. Stranks, M. M. Lee, G. Lanzani, H. J. Snaith, A. Petrozza, *Nat. Commun.* **2014**, 5, 3586.
- [15] M. A. Green, Y. Jiang, A. M. Soufiani, A. Ho-Baillie, *J. Phys. Chem. Lett.* **2015**, 6, 4774.
- [16] Y.-M. You, W.-Q. Liao, D. Zhao, H.-Y. Ye, Y. Zhang, Q. Zhou, X. Niu, J. Wang, P.-F. Li, D.-W. Fu, Z. Wang, S. Gao, K. Yang, J.-M. Liu, J. Li, Y. Yan, R.-G. Xiong, *Science* **2017**, 357, 306.
- [17] W. Y. Zhang, Y. Y. Tang, P. F. Li, P. P. Shi, W. Q. Liao, D. W. Fu, H. Y. Ye, Y. Zhang, R. G. Xiong, *J. Am. Chem. Soc.* **2017**, 139, 10897.
- [18] G. Xing, N. Mathews, S. S. Lim, N. Yantara, X. Liu, D. Sabba, M. Gratzel, S. Mhaisalkar, T. C. Sum, *Nat. Mater.* **2014**, 13, 476.
- [19] D. Li, G. Wang, H.-C. Cheng, C.-Y. Chen, H. Wu, Y. Liu, Y. Huang, X. Duan, *Nat. Commun.* **2016**, 7, 11330.
- [20] A. Jaffe, Y. Lin, C. M. Beavers, J. Voss, W. L. Mao, H. I. Karunadasa, *ACS Cent. Sci.* **2016**, 2, 201.
- [21] K. Matsuishi, T. Ishihara, S. Onari, Y. Chang, C. Park, *Phys. Status Solidi B* **2004**, 241, 3328.
- [22] F. Capitani, C. Marini, S. Caramazza, P. Postorino, G. Garbarino, M. Hanf and, A. Pisanu, P. Quadrelli, L. Malavasi, *J. Appl. Phys.* **2016**, 119, 185901.
- [23] G. Grancini, V. D'Innocenzo, E. R. Dohner, N. Martino, A. R. Srimath Kandada, E. Mosconi, F. De Angelis, H. I. Karunadasa, E. T. Hoke, A. Petrozza, *Chem. Sci.* **2015**, 6, 7305.
- [24] M. I. Saidaminov, A. L. Abdelhady, B. Murali, E. Alarousu, V. M. Burlakov, W. Peng, I. Dursun, L. Wang, Y. He, G. Maculan, *Nat. Commun.* **2015**, 6, 7586.
- [25] Y. Zhou, L. You, S. Wang, Z. Ku, H. Fan, D. Schmidt, A. Rusydi, L. Chang, L. Wang, P. Ren, *Nat. Commun.* **2016**, 7, 11193.
- [26] R. Cohen, N. Kitamura, Z. Fang, *Appl. Phys. Lett.* **1987**, 50, 1675.
- [27] K. Galkowski, A. Mitioglu, A. Miyata, P. Plochocka, O. Portugall, G. E. Eperon, J. T.-W. Wang, T. Stergiopoulos, S. D. Stranks, H. J. Snaith, *Energy Environ. Sci.* **2016**, 9, 962.
- [28] P. Peumans, A. Yakimov, S. R. Forrest, *J. Appl. Phys.* **2003**, 93, 3693.
- [29] M. Gerhard, A. P. Arndt, M. Bilal, U. Lemmer, M. Koch, I. A. Howard, *Phys. Rev. B* **2017**, 95, 195301.
- [30] M. Saba, M. Cadelano, D. Marongiu, F. Chen, V. Sarritzu, N. Sestu, C. Figus, M. Aresti, R. Piras, A. G. Lehmann, *Nat. Commun.* **2014**, 5, 5049.
- [31] L. A. Padilha, J. T. Stewart, R. L. Sandberg, W. K. Bae, W.-K. Koh, J. M. Pietryga, V. I. Klimov, *Nano Lett.* **2013**, 13, 1092.
- [32] A. Franceschetti, J. An, A. Zunger, *Nano Lett.* **2006**, 6, 2191.
- [33] D. Wake, H. Yoon, J. Wolfe, H. Morkoc, *Phys. Rev. B* **1992**, 46, 13452.
- [34] W. Kong, Z. Ye, Z. Qi, B. Zhang, M. Wang, A. Rahimi-Iman, H. Wu, *Phys. Chem. Chem. Phys.* **2015**, 17, 16405.
- [35] E. Mosconi, D. Meggiolaro, H. J. Snaith, S. D. Stranks, F. De Angelis, *Energy Environ. Sci.* **2016**, 9, 3180.
- [36] Y. D. Glinka, S. Babakiray, M. B. Holcomb, D. Lederman, *J. Phys.: Condens. Matter.* **2016**, 28, 165601.
- [37] R. J. Warburton, C. Schulhauser, D. Haft, C. Schäfer, K. Karrai, J. M. Garcia, W. Schoenfeld, P. M. Petroff, *Phys. Rev. B* **2002**, 65, 113303.
- [38] A. J. Bennett, R. B. Patel, J. Skiba-Szymanska, C. A. Nicoll, I. Farrer, D. A. Ritchie, A. J. Shields, *Appl. Phys. Lett.* **2010**, 97, 031104.
- [39] N. Grandjean, M. Leroux, M. Lügt, J. Massies, *Appl. Phys. Lett.* **1997**, 71, 240.
- [40] C. Kittel, *Introduction to Solid State Physics*, 7th ed., John Wiley & Sons, New York **1996**.
- [41] K. Park, Z. Deutsch, J. J. Li, D. Oron, S. Weiss, *ACS Nano* **2012**, 6, 10013.
- [42] N. W. Ashcroft, N. D. Mermin, *Solid State Physics*, Holt, Rinehart and Winston, New York **1976**.
- [43] Y. Wang, J. Xiao, H. Zhu, Y. Li, Y. Alsaïd, K. Y. Fong, Y. Zhou, S. Wang, W. Shi, Y. Wang, A. Zettl, E. J. Reed, X. Zhang, *Nature* **2017**, 550, 487.
- [44] I. Anusca, S. Balčiūnas, P. Gemeiner, Š. Svirskas, M. Sanjalp, G. Lackner, C. Fettkenhauer, J. Belovickis, V. Samulionis, M. Ivanov, B. Dkhil, J. Banys, V. V. Shvartsman, D. C. Lupascu, *Adv. Energy Mater.* **2017**, 7, 1700600.
- [45] A. Oshero, E. M. Hutter, K. Galkowski, R. Brenes, D. K. Maude, R. J. Nicholas, P. Plochocka, V. Bulovic, T. J. Savenije, S. D. Stranks, *Adv. Mater.* **2016**, 28, 10757.
- [46] Y. P. Varshni, *Physica* **1967**, 34, 149.
- [47] K. O'Donnell, X. Chen, *Appl. Phys. Lett.* **1991**, 58, 2924.
- [48] L. Vina, S. Logothetidis, M. Cardona, *Phys. Rev. B* **1984**, 30, 1979.
- [49] J. Yang, X. Wen, H. Xia, R. Sheng, Q. Ma, J. Kim, P. Tapping, T. Harada, T. W. Kee, F. Huang, *Nat. Commun.* **2017**, 8, 14120.
- [50] A. D. Wright, C. Verdi, R. L. Milot, G. E. Eperon, M. A. Pérez-Osorio, H. J. Snaith, F. Giustino, M. B. Johnston, L. M. Herz, *Nat. Commun.* **2016**, 7, 11755.
- [51] F. Cadiz, E. Courtade, C. Robert, G. Wang, Y. Shen, H. Cai, T. Taniguchi, K. Watanabe, H. Carrere, D. Lagarde, *Phys. Rev. X* **2017**, 7, 021026.